POLITECNICO DI TORINO
Repository ISTITUZIONALE

Reconfigurable multilevel control of hybrid all-dielectric phase-change metasurfaces

Original
Reconfigurable multilevel control of hybrid all-dielectric phase-change metasurfaces / de Galarreta, C.R., Sinev, I., Alexeev, A.M., Trofimov, P., Ladutenko, K., Carrillo, S.G.-C., Gemo, E., Baldycheva, A., Bertolotti, J., David Wright, C.. - In: OPTICA. - ISSN 2334-2536. - ELETTRONICO. - 7:5(2020), pp. 476-484. [10.1364/OPTICA.384138]

Availability:
This version is available at: 11583/2989995 since: 2024-06-28T20:56:48Z

Publisher:
Optica Publ.

Published
DOI:10.1364/OPTICA.384138

Terms of use:

This article is made available under terms and conditions as specified in the corresponding bibliographic description in the repository

Publisher copyright

(Article begins on next page)

09 November 2026

optica

Reconfigurable multilevel control of hybrid all-dielectric phase-change metasurfaces

Carlota Ruiz de Galarreta,[1] Ivan Sinev,[2] Arseny M. Alexeev,[1] Pavel Trofimov,[2] Konstantin Ladutenko,[2] Santiago Garcia-Cuevas Carrillo,[1] Emanuele Gemo,[1] Anna Baldycheva,[1] Jacopo Bertolotti,[1] and C. David Wright[1,*]

[1]College of Engineering Mathematics and Physical Sciences, University of Exeter, Exeter EX4 4QF, UK
[2]ITMO University, 197101 St. Petersburg, Russia
*Corresponding author: david.wright@exeter.ac.uk

Received 25 November 2019; revised 18 March 2020; accepted 5 April 2020 (Doc. ID 384138); published 7 May 2020

All-dielectric metasurfaces comprising arrays of nanostructured high-refractive-index materials are re-imagining what is achievable in terms of the manipulation of light. However, the functionality of conventional dielectric-based metasurfaces is fixed by design; thus, their optical response is locked in at the fabrication stage. A far wider range of applications could be addressed if dynamic and reconfigurable control were possible. We demonstrate this here via the novel concept of hybrid metasurfaces, in which reconfigurability is achieved by embedding sub-wavelength inclusions of chalcogenide phase-change materials within the body of silicon nanoresonators. By strategic placement of an ultra-thin $Ge_2Sb_2Te_5$ layer and reversible switching of its phase-state, we show individual, multilevel, and dynamic control of metasurface resonances. We showcase our concept via the design, fabrication, and characterization of metadevices capable of dynamically filtering and modulating light in the near infrared (O and C telecom bands), with modulation depths as high as 70% and multilevel tunability. Finally, we show numerically how the same approach can be re-scaled to shorter wavelengths via appropriate material selection, paving the way to additional applications, such as high-efficiency vivid structural color generators in the visible spectrum. We believe that the concept of hybrid all-dielectric/phase-change metasurfaces presented in this work could pave the way for a wide range of design possibilities in terms of multilevel, reconfigurable, and high-efficiency light manipulation.

Published by The Optical Society under the terms of the Creative Commons Attribution 4.0 License. Further distribution of this work must maintain attribution to the author(s) and the published article's title, journal citation, and DOI.

https://doi.org/10.1364/OPTICA.384138

1. INTRODUCTION

Optical metasurfaces offer a technologically important route toward the realization of lightweight and compact photonic devices with novel functionalities [1–5]. Ever since the concept of optical metasurfaces emerged, a number of novel photonic devices with exciting properties have been reported, including frequency selective surfaces and/or absorbers [6,7], flat lenses [8], polarizers [9], beam steerers [10], holograms, and more [1–3]. In such devices, subwavelength building blocks (often termed meta-atoms) supporting electric and/or magnetic resonances can be used as a designer interface for local engineering of the phase, amplitude, and polarization of light. The most promising platform for obtaining a strong magnetic response at optical frequencies is currently based on all-dielectric nanophotonics, in which the meta-atoms are made of high-refractive-index materials, such as silicon, germanium, or gallium phosphide [11–18]. Isolated nanoantennas (e.g., spheres or disks) of such materials support a series of scattering resonances (usually termed Mie resonances) of both electric and magnetic types [11]. The effective magnetic response in high-index all-dielectric nanoantennas is driven by displacement currents, rather than, as in the case of more conventional metal plasmonic metasurfaces, by conduction currents [11,15]. As a result, all-dielectric nanoantennas are also practically free from ohmic losses, leading to much higher efficiencies of operation when compared to plasmonic-based designs. In addition, the interaction of equally strong magnetic and electric dipole resonances, enabled by the use of dielectric meta-atoms, brings about a huge range of opportunities for the manipulation of light and vast degrees of freedom in terms of design [13,18–20].

However, the functionality of all-dielectric metamaterials and metasurfaces is generally fixed by design, i.e., the optical response is determined by the size, shape, spatial arrangement, and constituent material properties of the high-index dielectric nanoantennas used. A far wider array of potential applications could be addressed if dynamic and reconfigurable (i.e., fast, multilevel, and reversible) control of the dielectric metasurface properties could be achieved. However, the dynamic control of all-dielectric metasurfaces is a very under-explored topic (though some interesting approaches have been made, for example by embedding structures into a liquid

crystal matrix [21,22], or the tuning of silicon refractive index through ultrafast photoexcitation [23]). We here address this key omission by developing, to the best of our knowledge, novel hybrid all-dielectric metasurfaces, in which reconfigurable and multilevel control is achieved by embedding subwavelength inclusions of a switchable and tunable chalcogenide phase-change layer within the body of high-index all-dielectric nanoantennas. Chalcogenide phase-change materials (PCMs), such as the GeSbTe-based alloys, can be switched quickly (nanoseconds or less) [24] and repeatedly (up to 10^{15} cycles) [25] between amorphous and crystalline states (and even between intermediate phases) by appropriate thermal, optical, or electrical stimuli (each of those ultimately leading to thermally driven change of the structural phase) [26,27]. Such phase-state switching is non-volatile in nature (as opposed to the alternative phase-change material VO_2, which is volatile) [28,29] and results in a huge contrast in the complex refractive index, making chalcogenide PCMs very attractive for the creation of fast, energy-efficient (low-power consumption), dynamically reconfigurable optical devices and metasurfaces [30]. Indeed, a number of plasmonic-based metasurfaces incorporating PCMs have been reported [31–38], along with the direct structuring of PCMs to yield dielectric metasurfaces [39,40]. In the latter approach, however, the dielectric antennas are made entirely of chalcogenide material, necessitating the use of large PCM volumes that can degrade significantly the optical performance (i.e., lead to low efficiencies due to dielectric losses) of the device. Perhaps even more importantly, large PCM volumes also preclude the achievement of the high cooling rates (typically tens of degrees per nanosecond [27]) required for re-amorphization of the PCM (due to the characteristic low thermal conductivity of PCMs) [26,31].

In this paper, therefore, we propose and experimentally demonstrate a new class of dynamically reconfigurable and multilevel all-dielectric metasurfaces based on a hybrid of high-index nanoresonators, combined with deeply subwavelength-sized (down to $\sim\lambda_0/100$) inclusions of chalcogenide-based phase-change materials. We illustrate our concept by designing, fabricating, and experimentally characterizing hybrid Si nanocylinder/$Ge_2Sb_2Te_5$ devices that work at telecoms wavelengths as reconfigurable dual-band (O and C band) to mono-band (C band only) spectral filters/modulators. Unlike previous designs that were involving optically resonant arrays on top of PCM films [33], here we incorporate the PCM directly in the volume of the resonator. As we demonstrate below, this not only provides extremely efficient switching by enabling the use of very thin PCM layers, but it also allows us to selectively address/control metasurface resonances (specifically the electric dipole mode) by strategically positioning the PCM inclusions at the electric field anti-nodes. Moreover, laser-induced multilevel switching of the PCM between states results in independent, non-volatile, multilevel, and dynamically reconfigurable control of the resonant modes. This opens up the possibility of new design degrees of freedom and functionalities not achievable otherwise (e.g., with resonators fully made entirely of PCMs [39]).

Finally, we show scalability of our approach toward other spectral ranges and device functionalities via numerical simulations. In particular, by judicious choice of materials and structure geometry, we show reconfigurable color generation in the visible spectrum via hybrid metasurfaces that combine the high-index dielectric TiO_2 (rutile) with the novel, low-loss PCM Sb_2S_3 [41]. We believe hybrid dielectric/phase-change metasurfaces such as the ones proposed in this work, could open up a new route toward the design and realization of tunable optical metasurfaces with improved functionalities that have potential applications in numerous technologically important fields, ranging from telecommunications to consumer technology, security, and defense.

2. RESULTS

A. Design

An illustration of our proposed hybrid dielectric/PCM metasurface is shown in Fig. 1(a). In this case, it consists of an array of Si/$Ge_2Sb_2Te_5$ nanodisks arranged in a square lattice on top of a SiO_2 substrate. The choice of $Ge_2Sb_2Te_5$ (GST for short) as the PCM in our design is made for two main reasons; first, it has very

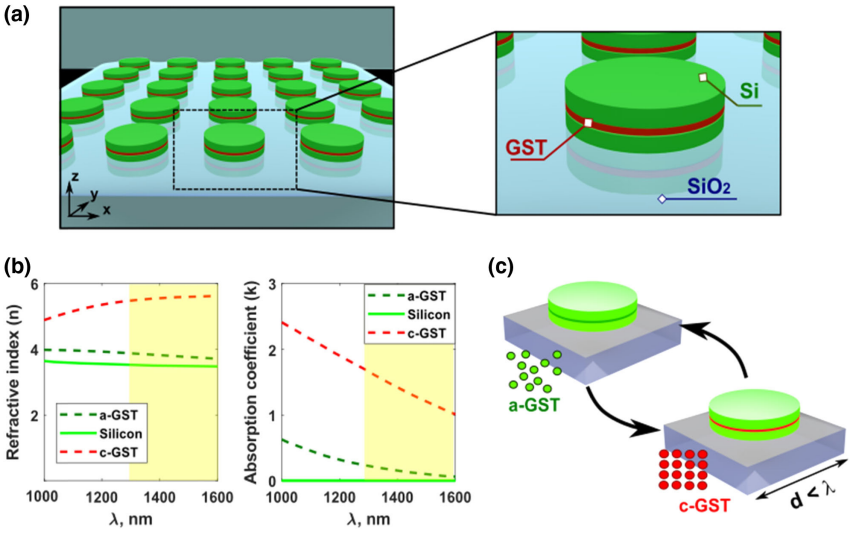

Fig. 1. (a) Schematics of the proposed hybrid silicon/PCM metasurface, consisting of arrays of silicon/GST nanodisks on a SiO_2 substrate in this example. (b) Refractive index (left) and the absorption coefficient (right) of amorphous GST (a-GST), crystalline GST (c-GST), and (amorphous) silicon. The spectral region of interest is highlighted in yellow: in this region, n and k of a-GST and silicon are closely matched. (c) Generic scheme of the device working principle: the hybrid silicon/GST cylinders effectively behave as silicon-only when the GST is amorphous, and the resonant modes supported by the array (thus its optical response) can be modified on demand by switching the GST layer between its amorphous and crystalline states.

attractive and well-known switching properties (such as the fast and repeatable switching, high optical contrast between states, etc., as described in the first paragraph), and second, its complex refractive index in the amorphous state, as shown in Fig. 1(b), matches very well the refractive index of (amorphous) silicon in the $\lambda = 1300$ nm to $\lambda = 1600$ nm window [31,42]. After crystallization of the GST, however, an increase of the refractive index n and absorption coefficient k takes place, with an overall increment of $\Delta n \sim 1.6$ and $\Delta k \sim 1.1$ in the spectral region of interest here. Therefore, our hybrid Si/GST nanodisks effectively behave as silicon-only cylinders when the GST is amorphous, but the resonant modes supported by the array (thus its optical response) can be modified on demand by switching the GST layer between its amorphous and crystalline states [Fig. 1(c)]. Importantly, due to the very small volume of PCM used in our approach, whether a mode is affected by switching of the PCM layer is critically dependent on, and can be controlled by, its particular placement within the overall resonator structure. This opens up the opportunity of selective and independent control of the metasurface modes by strategically positioning the PCM layer at the anti-nodes of the electric field.

To highlight the independent, reconfigurable control of metasurface resonances that is possible with the hybrid high-index dielectric/PCM concept, we now design, fabricate, and experimentally characterize devices suitable for simultaneous and tunable filtering/switching in the O and C telecommunications bands (1320 nm and 1550 nm, respectively). To create a metasurface with resonances in both these bands, we capitalize on the morphological dependence of Mie resonances of dielectric disks [16–19], which enables their mutual tuning through the change of the disk aspect ratio. Design and analysis of the devices was carried out employing finite element methods (FEM) using the commercial software package Comsol Multiphysics (see Supplement 1 Section 1 for a detailed description of FEM models).

The unit cell design of our devices is summarized in Fig. 2, where the period Λ is 850 nm, the cylinder thickness t_{cyl} is 195 nm, and the cylinder radius r is 666 nm. As shown in the reflectance spectrum R of Fig. 2(a), employing cylinders made exclusively of lossless Si (i.e., without the GST inclusion) results in two spectrally separated resonances falling at the O and C telecommunication bands, associated to the electric (ED) and magnetic (MD) dipole modes of a single disk [15,16], thus creating a dual-band filtering behavior. Replacing Si by GST [thus yielding all-GST nanodisks, see Fig. 2(b)] results in severe damping of the resonances in both amorphous (a-GST) and crystalline (c-GST) states, due to high PCM volume leading to large optical losses across the spectrum [as shown previously in Fig. 1(b)]. Indeed, such relatively high optical losses for the all-PCM approach lead to relatively low device efficiencies [39,40], similar in fact to those obtained with plasmonic phase-change metasurfaces [30–33]. Thus, an alternative approach to the use of direct structuring of PCMs to provide all-dielectric metasurfaces is needed, since the latter (1) does not provide any improvement, from an optical performance point of view, with respect to plasmonic PCM-based metasurfaces [39,40] and (2) requires large PCM volumes for which reversible switching becomes very challenging, if at all possible [26]. Remarkably, as we show in Fig. 2(c), by introducing an ultra-thin amorphous GST layer ($t_{gst} = 15$ nm) in the middle of a silicon resonator body,

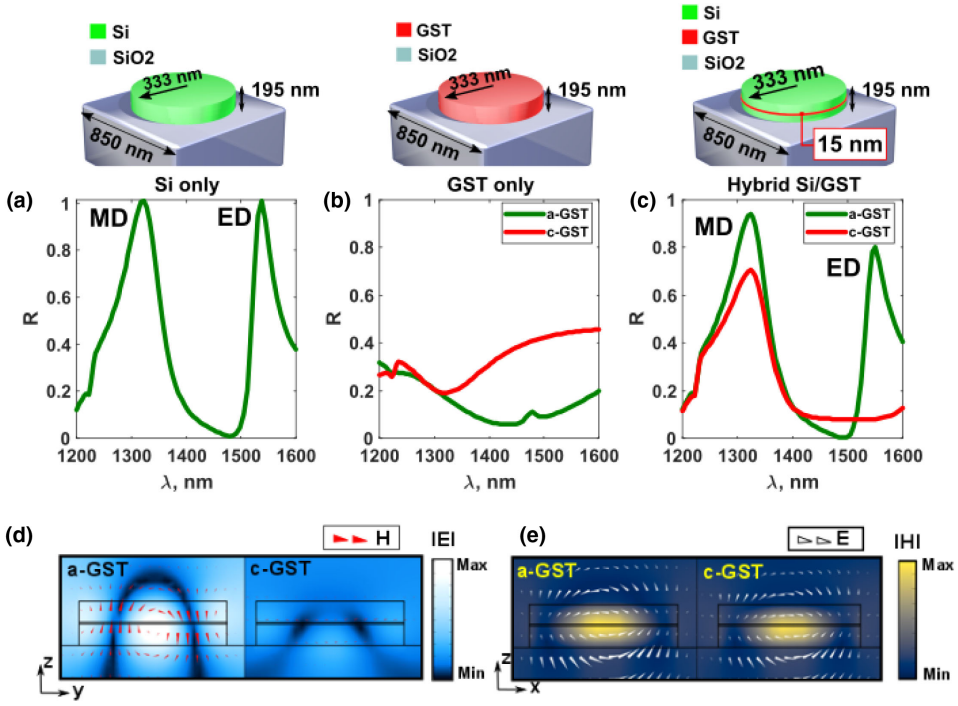

Fig. 2. (a) Schematics and dimensions of the unit cell of an array of cylinders fully made of silicon (top), and corresponding reflectance spectrum (bottom), showing a dual-band-filtering behavior where MD and ED are located at the O and C telecommunication bands. (b) Schematics and dimensions of the unit cell of arrays with direct structuring of GST (top), and corresponding reflectance spectrum for amorphous and crystalline states (bottom), where the optical response is degraded due to the presence of relatively high dielectric losses. (c) Schematics and dimensions of the unit cell considering a hybrid silicon/GST cylinder design (top), and corresponding reflectance spectrum (bottom) for amorphous and crystalline phases. The optical performance of silicon-only cylinders is maintained (green line), and selective control of the ED can be achieved via crystallization of the GST later (red line). (d) and (e) Electromagnetic field distribution of the electric (d) and magnetic (e) resonances for amorphous and crystalline phases of the GST.

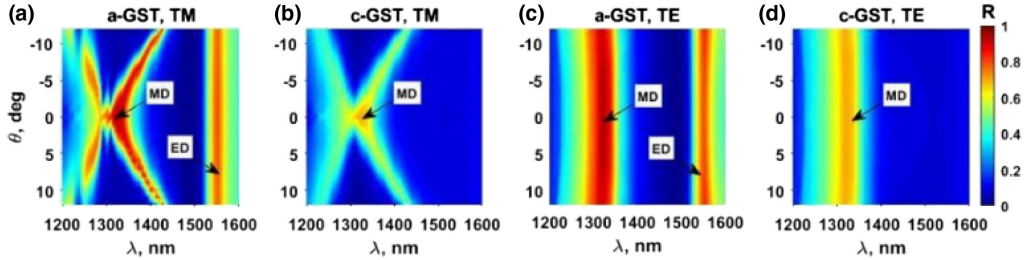

Fig. 3. (a) and (b) Angular reflectance under TM polarization for (a) amorphous and (b) crystalline states, showing splitting of the MD with the angle of incidence, and cancellation of the ED in the crystalline phase. (c) and (d) Angular reflectance under TE polarization for (c) amorphous and (d) crystalline states, showing a dispersionless behavior of the MD, and cancellation of the ED in the crystalline phase.

we can recover the dual-band resonant behavior achievable with silicon-only cylinders (apart from a small residual absorption; see Supplement 1 Section 2A). Moreover, crystallization of the GST layer reveals a quite different scenario [Fig. 2(c), red line]; here, the ED resonance is strongly attenuated, while the MD resonance remains mostly unaffected. The nature of such behavior can be readily explained by looking at the hybrid nanodisk near-field distributions at the resonant frequency of ED and MD modes shown in Figs. 2(d) and 2(c). Figure 2(d) (left) shows the characteristic electric field profile of an electric resonance when the GST is amorphous, with a strong enhancement of the electric field modulus in the center of the disk (see color bar) surrounded by magnetic current loops (red cones). After crystallization, the GST layer, being intentionally placed in the electric field antinodes of the mode, results in attenuation of this particular resonance, essentially due to an abrupt increase of the GST refractive index and absorption coefficient [Fig. 2(d), right]. Correspondingly, Fig. 2(e) (left) shows the typical magnetic field profile of a magnetic dipole mode, with a strong enhancement of the magnetic field modulus in the disk center (see color bar), surrounded by electric field loops (white cones). Here, the electric fields interaction with the GST layer is much weaker, leading to almost no attenuation of this mode upon switching to its crystalline phase [as shown in Fig. 2(e) (right) and in more detail in Supplement 1 Section 2.A].

The above-described results clearly show that our hybrid Si/GST metasurface can operate as a reconfigurable dual-band to mono-band spectral filter, via selective cancelation of one of the resonant modes (ED), without altering the other (MD). With the GST layer in the amorphous state, both O and C band wavelengths (1320 and 1550 nm) are reflected, whereas switching the GST to its crystalline state results in a single-band filter in which, effectively, only the O band is reflected (with the C band being transmitted instead). The absolute modulation depth in reflection ($M_{\mathrm{DR}} = R_{\mathrm{am}} - R_{\mathrm{cr}}$) is 72% at $\lambda = 1550$ nm (relative modulation contrast $|R_{\mathrm{am}} - R_{\mathrm{cr}}|/R_{\mathrm{cr}} = 100\%$). In transmission, the modulation depth at the same wavelength is $M_{\mathrm{DT}} = T_{\mathrm{am}} - T_{\mathrm{cr}} = 65\%$ (see Supplement 1 Section 2B).

Finally, we also investigated the robustness of our device performance against changing the angle of incidence. For this purpose, we calculated reflection for a range of angles of incidence θ going from $-13°$ to $13°$ in steps of $\Delta\theta = 0.5°$ for both transverse electric (TE) and transverse magnetic (TM) polarization states. Figures 3(a) and 3(b) show the angular dependence of the reflectance spectra under TM excitation for a-GST and c-GST, respectively. It can be seen from Fig. 3(a) that the mode associated with the ED resonance of the disk is dispersionless (i.e., remains stationary when varying θ), whereas the MD-associated mode for non-zero angles of incidence splits into two separate Bloch modes with a high dispersion and opposite sign of group velocity due to strong interaction between the disks (see the eigenmode analysis in Supplement 1 Section 2C and [43,44]). Crystallization of the GST layer results, as expected, in the cancellation of the ED mode for every angle of incidence, while the splitting of the MD mode is conserved. For TE-polarized excitation [see Figs. 3(c) and 3(d) for a-GST and c-GST cases, respectively], both ED- and MD-associated modes remain unaffected by the oblique incidence, while maintaining the characteristic cancellation of the ED mode after GST crystallization. These results suggest that our metasurfaces can therefore have additional features (such as tunable multiband filtering) upon exciting the device at different angles under TM polarization. On the other hand, angular robustness could be achieved by simply changing the incident polarization state to TE.

B. Hybrid Silicon/GST Fabrication and Characterization

The hybrid Si/PCM device designs shown in Fig. 2(c) were fabricated in areas of 100 μm × 100 μm using the magnetron thin-film sputter deposition, e-beam lithography, and etching techniques, as described in the methods section (a schematic flowchart of the whole process can be found in Supplement 1 Section 3). A scanning electron microscope (SEM) image of a typical as-fabricated device is depicted in Fig. 4(a), showing measured nanodisk diameters of 668 nm extremely close (in fact within the measurement error) of the target design diameter [as in Fig. 2(c)] of 666 nm. The devices were optically characterized using back focal plane spectroscopy (described in the methods section and Supplement 1 Section 4) to obtain the experimental reflectance spectra. Results, for normal incidence, are shown in Fig. 4(b) and show excellent agreement with the simulated results previously shown in Fig. 2(c). For a-GST [green curves in Fig. 4(b)], a reflectance peak of 79% corresponding to the electric dipole resonance is clearly observed at $\lambda = 1540$ nm (*cf.* 80% at $\lambda = 1550$ nm from numerical simulations). As expected, a second reflectance peak corresponding to the magnetic dipole is located experimentally at a shorter wavelength of $\lambda = 1380$ nm, with a strength of $R = 83\%$ (*cf.* $\lambda = 1320$ and $R = 93\%$ obtained numerically). The reflectance spectrum taken after (hot plate) crystallization (red curve) confirms the predicted absence of the ED peak at $\lambda = 1540$ nm, with the MD nearly unaffected by the phase transition. An absolute experimental contrast (modulation depth) between phases of 70% was obtained at $\lambda = 1540$ nm, very close to that predicted by our numerical models (i.e., 72% at $\lambda = 1550$ nm).

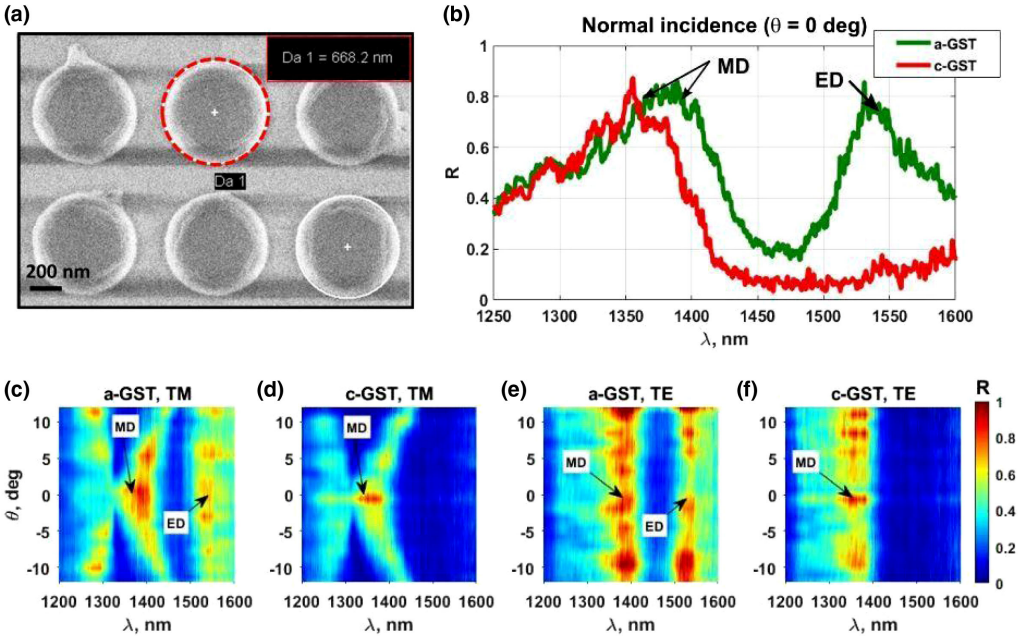

Fig. 4. Measured optical response of the fabricated meta-devices. (a) SEM image of (part of) a typical as-fabricated hybrid silicon/GST all-dielectric metasurface device, here showing six unit cells. (b) Experimentally obtained reflectance spectra for the as-fabricated device with the GST layer in both amorphous and crystalline states. (c)–(f) Experimentally measured angular reflectance spectra: (c) and (d) under TM excitation when the GST is (c) amorphous and (d) crystalline; (e) and (f) under TE excitation when GST is (e) amorphous and (f) crystalline. The experimental angular reflectance spectra show good agreement with simulation [as in Figs. 3(c)–3(f)] and confirm robustness of device performance against the angle of incidence for TE illumination, but dispersion of the MD-associated mode with the angle for TM illumination.

The optical performance of our hybrid metasurfaces at oblique incidence was also experimentally investigated, under both TE and TM incidence, and compared to our numerical simulations. Thus, Figs. 4(c)–4(f) show the experimentally measured reflectance spectra as a function of the angle of incidence under both TM and TE polarization and for amorphous and crystalline states of the GST layer. As predicted by simulations shown in Figs. 3(a) and 3(b), under TM illumination, our as-fabricated metasurfaces exhibit splitting with the angle of incidence of the MD and no dispersion of the ED mode [Fig. 4(a)], along with the cancellation of the ED mode upon GST crystallization [Fig. 4(b)]. Under TE illumination, again, an excellent agreement between the simulations [Figs. 3(c) and 3(d)] and experiment [Figs. 4(c) and 4(d)] was achieved, showing robustness at oblique incidence (i.e., ED and MD reflection peaks remain in the same spectral position at every angle), and the ED resonance at 1550 nm is completely suppressed for the c-GST phase over the entire range of incident angles measured (here to ±12.5°).

C. Optically Induced, Multilevel, Reversible Switching of Hybrid Silicon/PCM Metasurfaces

Our novel hybrid all-dielectric/PCM metasurface approach also enables rapid, reversible, multilevel, and non-volatile switching of the resonances, which we demonstrate here by employing femtosecond laser scans [45–47]. We use pulses with a central wavelength of 1050 nm, as described in the methods section. At this wavelength, the losses of both amorphous and crystalline

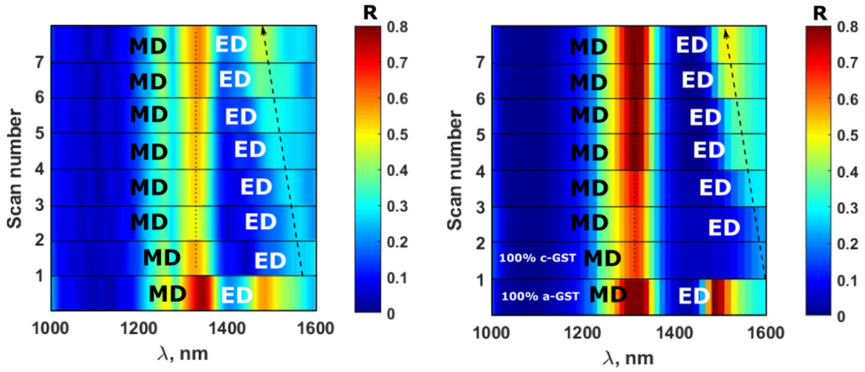

Fig. 5. (a) Experimental demonstration of multilevel tuning of the hybrid silicon/GST metasurface. Starting from the as-deposited amorphous state (bottom panel), the metasurface is first switched to the crystalline state (Scan 1) by excitation with a train of laser pulses with a fluence of 1.28 mJ/cm^2. Multilevel switching from the fully crystalline state back to amorphous GST (Scans 2 to 7) was carried out using a single-pulse regime with fluences linearly increasing from 6.4 up to 19.2 mJ/cm^2. (b) FEM simulation of the multilevel switching process (see Supplement 1 Section 7).

GST are reasonably high, while the absorption in silicon is negligible, which ensures very effective heating of GST inclusion. Importantly, we successfully demonstrate a reversible and multilevel tuning of the GST phase between fully crystalline and fully amorphous states, which in turn leads to the possibility of fine control over the spectral position and amplitude of the metasurface resonance.

Experimental results are given in Fig. 5(a) where microreflectivity measurements at various stages of the multilevel switching cycle (here seven states, but 10 states also demonstrated in Supplement 1 Section 5) are shown. The switching to the crystalline state from the initially as-deposited amorphous state [Scan 1 in Fig. 5(a)] was performed using multipulse excitation (repetition rate 80 MHz) with a fluence of 1.28 mJ/cm^2. Multilevel switching from crystalline GST back to amorphous GST [Scans 2 to 7 in Fig. 5(a)] was carried out using a single-pulse regime with fluences linearly increasing from 6.4 up to 19.2 mJ/cm^2. Figure 5(a) clearly indicates a gradual restoration and blue shift of the ED resonance as the GST layer is gradually re-amorphized. In fact, we were able to reconstruct the multilevel switching process via COMSOL simulations [shown for comparison in Fig. 5(b)], which suggest that the multilevel tuning is achieved by redistribution of the hot spots at the laser pump wavelength, resulting in different regions being re-amorphized after each scan (details of these simulations can be found in Supplement 1 Section 6).

3. DEVICE SCALABILITY: TOWARD HIGH-EFFICIENCY VIVID NON-VOLATILE COLOR GENERATORS

As a final example of the broad general scope of our hybrid all-dielectric/PCM metasurface concept, we show its potential for tunable color generation, which could have applications for non-volatile digital paper, transmissive or reflective displays, electronic signage, and reconfigurable spectral filtering. Indeed, phase-change materials in the form of resonant cavities and/or combined with plasmonic metasurfaces have been already successfully employed to produce tunable color generation [41, 48–50]. However, most of the reported approaches are limited to operating in reflection only [41,49], and performance is limited by plasmonic and dielectric losses coming from metallic parts and phase-change materials, respectively. As we will show in this section, employing

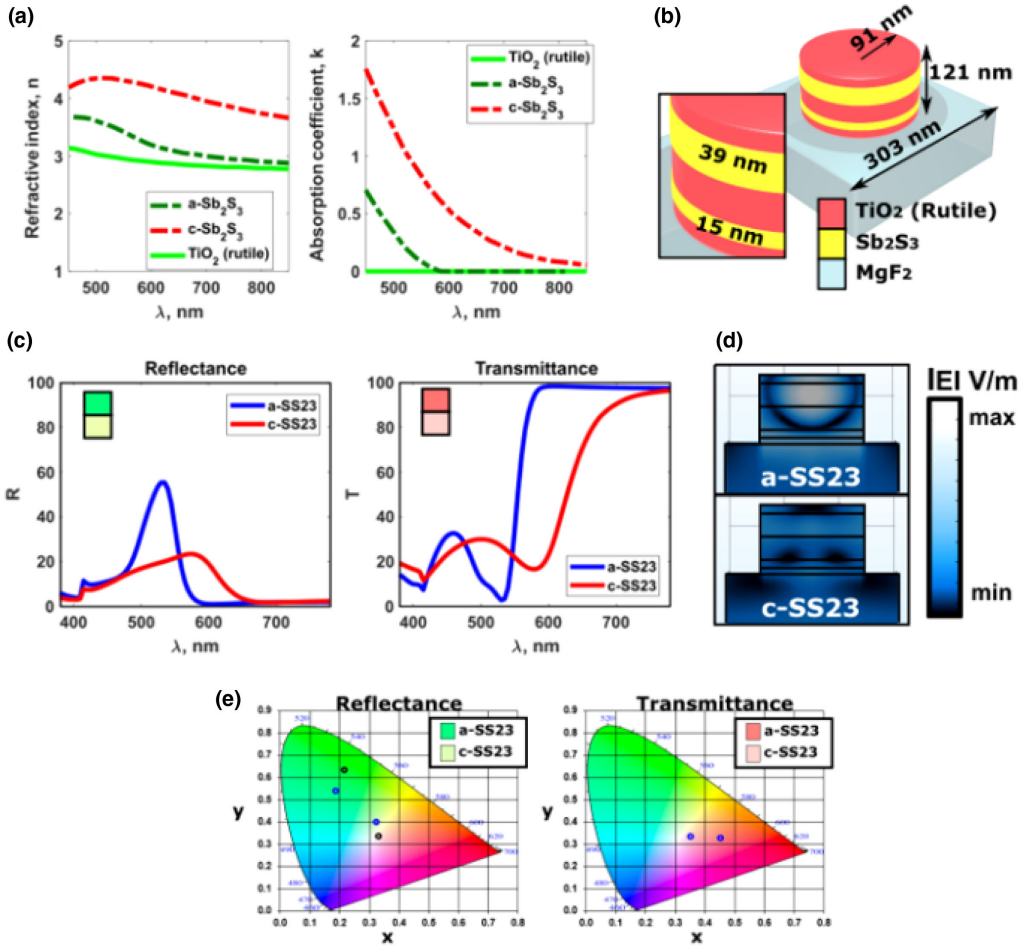

Fig. 6. (a) Refractive index and absorption coefficient of TiO_2 (rutile), amorphous and crystalline Sb_2S_3 ($a-Sb_2S_3$ and $c-Sb_2S_3$), taken from [41,51]. (b) Schematics of the hybrid TiO_2/Sb_2S_3 nanocylinder, showing geometrical dimensions and the PCM distribution in the optimized structure. (c) Reflectance (left) and transmittance (right) spectra for amorphous and crystalline Sb_2S_3 states. Insets show the resultant color, based on chromaticity calculations employing a standard D65 illuminant. (d) Electric field distribution for amorphous (top) and crystalline (bottom) Sb_2S_3, excited at a wavelength of $\lambda = 520$ nm, confirming attenuation of the ED mode after crystallization. (e) Chromaticity objective coordinates (black dots) and obtained coordinates (blue dots) in reflection (left), and subsequent resulting coordinates in transmission (right).

hybrid phase-change dielectric metasurfaces could lead to high-efficiency, reconfigurable structural color generation, operating simultaneously in reflection and transmission.

The basic structure here again consists of a lossless dielectric nanocylinder with embedded PCM layers. Here, for the PCM layer, we use the material Sb_2S_3 (SS23 for short), which has low losses (in the amorphous phase) in the visible spectrum (as compared to say GST in particular) [41]. For the dielectric of the nanocylinders, we use TiO_2 here (rutile [51]), which has a near matching of refractive index to amorphous SS23 [see Fig. 6(a)]. The overall structure is shown in Fig. 6(b) (note that we use MgF_2 here as a substrate to avoid the generation of diffraction orders across the entire visible spectrum, due to its low refractive index, $n_{MgF2} = 1.38$). As in the case of the Si/GST nanocylinder design described above, when the SS23 is in its amorphous (i.e., low optical loss) state, this hybrid metasurface can be tuned to generate high-efficiency reflectivity resonances. As shown in Fig. 6(c) (left), a sharp reflectance peak of a 60% efficiency is excited at $\lambda = 520$ nm when the SS23 PCM is amorphous, which results in a vivid primary additive color in reflection (here green). After crystallization, however, the resonance is shifted and damped due to an abrupt increase of the refractive index and absorption coefficient, resulting in a pale, close to white, color appearance. Again, as in the case for the Si/GST devices described previously, such behavior was achieved by positioning the SS23 material coincident with the electric field maxima under resonance, as shown in Fig. 6(d). It is worth highlighting, however, that here we did not directly choose the position and thicknesses of the tunable layers, but instead, we allowed an optimization tool (running in MATLAB) to find the optimum position for the generation of a strong green color in reflection. It is reassuring to note that the optimization routine placed the PCM layers at precisely the same positions that we would have chosen considering the location of field maxima.

Figure 6(e) shows the chromaticity color coordinates obtained in the reflection and transmission after the optimization of the cylinder geometrical parameters (a detailed description of the optimization process and color space calculations can be found in Supplement 1 Section 7), confirming pure green (reflection) and magenta (transmission) colors when the SS23 layer is amorphous, and a close to white state after crystallization. Additional colors could be generated via appropriate optimization of the cylinder geometry and the position of the PCM inclusions using the same optimization routine described in Supplement 1 Section 7. Furthermore, alternative PCMs exhibiting low losses in the visible spectrum, such as gallium lanthanum sulphide [52], are available, as well as other high-index dielectrics, such as hydrogenated silicon, thus increasing even more the design degrees of freedom when it comes to color generation.

4. METHODS

A. Device Fabrication

Arrays of nanodisks were fabricated on 1 cm × 1 cm SiO_2 substrates, previously cleaned with acetone and rinsed in isopropyl alcohol. First, a silicon/GST/silicon tri-layer stack was deposited using a magnetron sputtering system (Nordiko). RF sputtering in an argon atmosphere (50 sccm) with a plasma power of 200 W was used to deposit the top and bottom silicon layers. DC sputtering was employed for the GST deposition, under the same atmosphere and a plasma power of 20 W. The chamber pressure and base vacuum for both processes were 8.5×10^{-2} and 1.0×10^{-5} Pa, respectively.

Next, the samples were covered with an adhesion layer (Ti-Prime) using a spinner at 4000 rpm for 20 s, with subsequent post-baking at 90°C for 5 min. A negative resist (ma-N 2403) was then spin-coated at 2500 rpm for 60 s and post-baked at 90°C for 10 min. Finally, a thin layer of conductive resist (Elecktra) was spin-coated to ease the charge dissipation during e-beam lithography (2500 rpm for 50 s, post-baking at 90°C for 2 min).

The required array pattern was then transferred to the resist via e-beam lithography (NanoBeam nB4), and subsequent development in MF-319 solution for 45 s was carried out to remove the unexposed areas. After lithography, the sample was post-baked at 90°C for 5 min to increase the hardness of the remaining exposed areas.

Finally, the samples were etched in a SF_6 and O_2 plasma mixture using an inductively coupled plasma-reactive ion etching (ICP-RIE) system. ICP (300 W) was used to create high-density plasma, which was then accelerated toward the sample by the RIE (200 W) component to achieve directional etching. A low pressure of 2 Pa was used to avoid frequent collisions inside the plasma cloud.

B. Optical Characterization

Optical properties of the metasurfaces were characterized using a back focal plane spectroscopy setup (a detailed description of this setup can be found in Supplement 1 Section 4). Sample excitation was provided by a linearly polarized beam from a supercontinuum laser source (Fianium SC400-6), which was carefully filtered and attenuated to ensure that GST inclusions do not change phase during the experiment. The beam was then focused on the sample using a 10× objective (Mitutoyo M Plan Apo NIR, NA = 0.26). The end facet of a multimode fiber (50 μm core, NA = 0.22) was manually scanned along the two main axes of the reflected light spot in the back focal plane of the optical setup with a step of 100 μm. Light collected by the fiber was then sent to a spectrometer (Horiba LabRAM HR800) equipped with water-cooled CCD (Andor iDus InGaAs) with a sensitivity range up to 1650 nm. This provided the metasurface reflectance spectra for both TE and TM polarizations, with an angle of incidence resolution of approximately 1 deg. The spectra were normalized to the reflectance of a protected silver mirror (Thorlabs, >97.5% reflectance in the spectral range of interest).

C. Femtosecond Optical Switching

Optical-switching experiments were carried out using a femtosecond laser source (Yb3+ Avesta TEMA-150, central wavelength 1050 nm, pulse duration 150 fs). To facilitate fast switching of large areas of the metasurface, the laser was focused on the sample with a 5 cm achromatic doublet lens that provided a smooth laser intensity profile in the focal plane (with a laser spot FWHM of approximately 15 μm). The sample was then scanned with respect to the laser beam to achieve switching of even larger areas of the metasurface. For these studies, we used the metasurface with a slightly lower diameter of the disks (311 nm) so that the position of the ED peak for both crystalline and amorphous states fitted into the spectral range of detection of our InGaAs CCD (up to 1650 nm).

5. CONCLUSION

We have introduced and experimentally validated a new concept in all-dielectric optical metasurfaces based on a hybrid combination of high-index dielectric building blocks with embedded subwavelength inclusions of chalcogenide phase-change materials. By using this hybrid approach, we are able not only to provide on-demand dynamic control of light amplitude, but also to deliver a very high efficiency of operation over a very wide spectral range by a judicious material choice. We demonstrated the flexibility and universality of our approach by the design and development of hybrid metasurfaces for applications as switchable spectral filters in the near-infrared and dynamic color generation in the visible spectrum.

For the spectral filtering application, we proposed and experimentally demonstrated $Si/Ge_2Sb_2Te_5$ hybrid metasurfaces consisting of arrays of low-aspect-ratio nanocylinders in which the magnetic and electric dipole resonances are specifically designed to be located at the telecommunication O and C bands ($\lambda = 1320$ nm and 1550 nm, respectively). This meta-device has dual-band filtering/modulation capabilities when the $Ge_2Sb_2Te_5$ layer is amorphous, but switches to a single-band configuration after crystallization, due to individual cancellation of the ED mode only (made achievable via strategic location of the PCM inclusions). Fabricated devices performed very much in line with theoretical (numerical) simulations, with an experimental contrast in reflection of 70% at 1540 nm obtained, using a GST layer of only 15 nm in thickness ($\sim\lambda_0/100$). This device has, to the best of our knowledge, the highest contrast/volume relationship reported for any PCM-based optical metasurface. Perhaps more importantly, the ability to use ultra-thin PCM layers in our hybrid metasurface approach is a critical factor in terms of ensuring a successful re-amorphization process, which requires cooling rates of the order of tens of degrees per nanosecond, rates that are unachievable when using large PCM volumes (due to the relatively low thermal conductivity of phase-change materials) [23,24,31]. Indeed, the use of ultra-thin PCM layers enabled us to write, using a femtosecond laser, reversible multilevel states in the phase-change layer, thus delivering the capability for ultra-fine dynamic control over the spectral position and amplitude of the metasurface resonance.

Finally, we have also demonstrated hybrid dielectric/PCM metasurfaces for operation in the visible spectrum, here for tunable non-volatile color generation in reflection and/or transmission. For this purpose, we used subwavelength inclusions of the low-loss (when in the amorphous phase) PCM Sb_2S_3 [41] in combination with the high-index dielectric rutile (TiO_2) to generate vivid and high-efficiency structural colors (by engineering the spectral position of the reflectivity resonances). Switching the Sb_2S_3 to its lossy crystalline state results in resonance damping/shifting, broadening the reflectance and transmittance spectra, thus generating a colorless (white) state. Our hybrid metasurfaces therefore also show potential for the realization of non-volatile digital paper, transmissive or reflective displays, and spectral filtering in the visible regime.

In summary, we have introduced a novel concept in dynamically reconfigurable optical metasurfaces, comprising a hybrid combination of high-index dielectrics and chalcogenide phase-change materials. Our approach can provide a practicable platform for the realization of a new generation of active optical metasurfaces with new and improved functionalities, with potential applications in numerous technologically important fields, ranging from telecommunications to consumer technology, and security and defense.

Funding. Engineering and Physical Sciences Research Council (EP/L015331/1, EP/M015130/1, EP/M015173/1); Russian Science Foundation (19-72-10086); Russian Foundation for Basic Research (18-32-00527).

Acknowledgment. C.D.W. acknowledges funding of the EPSRC Chalcogenide Advanced Manufacturing Partnership (ChAMP) and Wearable and Flexible Technologies (WAFT) projects. C.R.d.G. acknowledges funding via the EPSRC CDT in metamaterials. Laser-driven switching experiments were performed with the support of Russian Science Foundation. I.S., P.T., and A.M.A. acknowledge the support from the RFBR for angle-resolved reflectance measurements. A.M.A acknowledges support from the EPSRC Impact Acceleration Account. The authors are grateful to Andrey Bogdanov for useful discussions.

Disclosures. The authors declare no conflicts of interest.

See Supplement 1 for supporting content.

REFERENCES

1. N. Yu and F. Capasso, "Flat optics with designer metasurfaces," Nat. Mater. **13**, 139–150 (2014).
2. S. B. Glybovski, S. A. Tretyakov, P. A. Belov, Y. S. Kivshar, and C. R. Simovski, "Metasurfaces: from microwaves to visible," Phys. Rep. **634**, 1–72 (2017).
3. A. V. Kildishev, A. Boltasseva, and V. M. Shalaev, "Planar photonics with metasurfaces," Science **339**, 1232009 (2013).
4. H.-T. Chen, A. T. Taylor, and N. Yu, "A review of metasurfaces: physics and applications," Rep. Prog. Phys. **79**, 076401 (2016).
5. G. Ding, Y. Yang, R. A. Deshpande, and S. I. Bozhevolnyi, "A review of gap surface plasmon metasurfaces: fundamentals and applications," Nanophotonics **7**, 1129–1156 (2018).
6. D. N. Jones, N. Liu, B. Corbett, P. Lovera, A. J. Quinn, and A. O'Riordan, "Surface plasmon assisted extraordinary transmission in metallic nanohole arrays and its suitability as a bio sensor," J. Phys. Conf. Ser. **307**, 012005 (2011).
7. A. Tittl, P. Mai, R. Taubert, D. Dregely, N. Liu, and H. Giessen, "Palladium-based plasmonic perfect absorber in the visible wavelength range and its application to hydrogen sensing," Nano Lett. **11**, 4366–4369 (2011).
8. F. Aieta, P. Genevet, M. A. Kats, N. Yu, R. Blanchard, G. Zeno, and F. Capasso, "Aberration-free ultrathin flat lenses and axicons at telecom wavelengths based on plasmonic metasurfaces," Nano Lett. **12**, 4932–4936 (2012).
9. C. Han and W. Y. Tam, "Broadband optical magnetism in chiral metallic nanohole arrays by shadowing vapor deposition," Appl. Phys. Lett. **106**, 081102 (2016).
10. L. Zou, W. Withayachumnankul, M. C. Shah, A. Mitchell, M. Bhaskaran, S. Sriram, and C. Fumeaux, "Dielectric resonator nanoantennas at visible frequencies," Opt. Express **21**, 1344–1352 (2013).
11. A. I. Kuznetsov, A. E. Miroshnichenko, Y. H. Fu, J. Zhang, and B. Luk'yanchuk, "Magnetic light," Sci. Rep. **2**, 492 (2012).
12. A. B. Evlyukhin, S. M. Novikov, U. Zywietz, R. L. Eriksen, C. Reinhardt, S. I. Bozhevolnyi, and B. N. Chichkov, "Demonstration of magnetic dipole resonances of dielectric nanospheres in the visible region, Nano Lett. **12**, 3749–3755 (2012).
13. A. I. Kuznetsov, A. E. Miroshnichenko, M. L. Brongersma, Y. S. Kivshar, and B. Lukyanchuk, "Optically resonant dielectric nanaostructures," Science **354**, aag2472 (2016).
14. J. Cambiasso, G. Grinblat, Y. Li, A. Rakovich, E. Cortes, and S. A. Maier, "Bridging the gap between dielectric nanophotonics and the visible

regime with effectively lossless gallium phosphide antennas," Nano Lett. **17**, 1219–1225 (2017).
15. I. Staude, A. E. Miroshnichenko, M. Decker, N. T. Fofang, S. Liu, E. Gonzales, J. Dominguez, T. S. Luk, D. N. Neshev, I. Brener, and Y. Kivshar, "Tailoring directional scattering through magnetic and electric resonances in subwavelength silicon nanodisks," ACS Nano. **7**, 7824–7832 (2013).
16. M. Decker, I. Staude, M. Falkner, J. Dominguez, D. N. Neshev, I. Brener, T. Pertsch, and Y. S. Kivshar, "High-efficiency dielectric Huygen's surfaces," Adv. Opt. Mater. **3**, 813–820 (2015).
17. Y. H. Fu, A. I. Kuznetsov, A. E. Miroshnichenko, Y. F. Yu, and B. Luk'yanchuk, "Directional visible light scattering by silicon nanoparticles," Nat. Commun. **4**, 1527 (2013).
18. R. Paniagua-Domínguez, Y. F. Yu, A. E. Miroschnichenko, L. A. Krivitsky, Y. H. Fu, V. Valuckas, L. Gonzaga, Y. T. Toh, A. Y. S. Kay, B. Luk'yanchuk, and A. I. Kuznetsov, "Generalised Brewster effect in dielectric metasurfaces," Nat. Commun. **7**, 10362 (2016).
19. Y. F. Yu, A. Y. Zhu, R. Paniagua-Dominguez, Y. H. Fu, B. Luk'yanchuk, and A. I. Kuznetsov, "High-transmission dielectric metasurfaces with 2π phase control at visible wavelengths," Laser Photon. Rev. **9**, 412–418 (2015).
20. R. Paniagua-Domínguez, Y. F. Yu, E. Khaidarov, S. Choi, V. Leong, R. M. Bakker, X. Liang, Y. H. Fu, V. Valuckas, L. A. Krivitsky, and A. I. Kuznetsov, "A metalens with a near-unity numerical aperture," Nano Lett. **18**, 2124–2132 (2018).
21. J. Sautter, I. Staude, M. Decker, E. Rusak, D. Neshev, I. Brener, and Y. S. Kivshar, "Active tuning of all-dielectric metasurfaces," ACS Nano. **9**, 4308–4315 (2015).
22. A. Komar, Z. Fang, J. Bohn, J. Sautter, M. Decker, A. Miroschnichenko, T. Pertsch, I. Brener, Y. S. Kivshar, I. Staude, and D. N. Neshev, "Electrically tunable all-dielectric optical metasurfaces based on liquid crystals," Appl. Phys. Lett. **110**, 071109 (2017).
23. S. Makarov, S. Kudryashov, I. Mukhin, A. Mozharov, V. Milichko, A. Krasnok, and P. Belov, "Tuning of magnetic optical response in a dielectric nanoparticle by ultrafast photoexcitation of dense electron-hole plasma," Nano Lett. **15**, 6187–6192 (2015).
24. D. Loke, T. H. Lee, W. J. Wang, L. P. Shi, R. Zhao, Y. C. Yeo, T. C. Chong, and S. R. Elliott, "Breaking the speed limits of phase-change memory," Science **336**, 1566–1569 (2012).
25. I. S. Kim, "High performance PRAM cell scalable to sub-20nm technology with below 4F2 cell size, extendable to DRAM applications," in *IEEE Symposium on VLSI Technology*, IEEE, Honolulu, Hawaii, USA, 2010, p. 203.
26. J. Siegel, A. Schropp, J. Solis, C. N. Alfonso, and M. Wuttig, "Rewritable phase-change optical recording in $Ge_2Sb_2Te_5$ films induced by picosecond laser pulses," Appl. Phys. Lett. **84**, 2250–2252 (2004).
27. M. Wuttig and N. Yamada, "Phase-change materials for rewritable data storage," Nat. Mater. **6**, 824–832 (2007).
28. M. R. Hashemi, S.-G. Yang, T. Wang, N. Sepulveda, and M. Jarrahi, "Electronically-controlled beam-steering through vanadium dioxide metasurfaces," Sci. Rep. **6**, 35429 (2016).
29. M. Kim, J. Jeoing, J. K. S. Pooon, and G. V. Eleftheriades, "Vanadium-dioxide-assisted digital optical metasurfaces for dynamic wavefront engineering," J. Opt. Soc. Am. B **33**, 980–988 (2016).
30. M. Wuttig, H. Bhaskaran, and T. Taubner, "Phase-change materials for non-volatile photonic applications," Nat. Photonics **11**, 465–476 (2017).
31. C. Ruiz de Galarreta, A. M. Alexeev, Y.-Y. Au, M. Lopez-Garcia, M. Klemm, M. Cryan, J. Bertolotti, and C. D. Wright, "Nonvolatile reconfigurable phase-change metadevices for beam steering in the near infrared," Adv. Funct. Mater. **28**, 1704993 (2018).
32. B. Gholipour, J. Zhang, K. F. MacDonald, D. W. Hewak, and N. I. Zheludev, "An all-optical, non-volatile, bidirectional, phase-change meta-switch," Adv. Mater. **25**, 3050–3054 (2013).
33. A. Tittl, A. K. U. Michel, M. Schaferling, X. Yin, B. Gholipour, L. Cui, M. Wuttig, T. Taubner, F. Neubrech, and H. Giessen, "A switchable mid-infrared perfect absorber with multispectral thermal imaging capability," Adv. Mater. **27**, 4597–4603 (2015).
34. L. Trimby, A. Baldycheva, and C. D. Wright, "Phase-change band-pass filters for multispectral imaging," Proc. SPIE **10541**, 105412B (2018).
35. S. Garcia-Cuevas Carrillo, G. R. Nash, H. Hasan, M. J. Cryan, M. Klemm, H. Bhaskaran, and C. D. Wright, "Design of practicable phase-change metadevices for near-infrared absorber and modulation applications," Opt. Express **24**, 13563–13573 (2016).
36. X. Tian and Z. Li, "Visible-near infrared ultra-broadband polarisation-independent metamaterial perfect absorber involving phase-change materials," Opt. Express **4**, 146–152 (2016).
37. P. Hosseini, C. D. Wright, and H. Bhaskaran, "An optoelectronic framework enabled by low-dimensional phase-change films," Nature **511**, 206–211 (2014).
38. X. Yin, T. Steinle, L. Huang, T. Taubner, M. Wuttig, T. Zentgraf, and H. Giessen, "Beam switching and bifocal zoom lensing using active plasmonic metasurfaces," Light Sci. Appl. **6**, e17016 (2017).
39. J. Tian, H. Luo, Y. Yang, F. Ding, Y. Qu, D. Zhao, M. Qiu, and S. I. Bozhevolnyi, "Active control of anapole states by structuring the phase-change alloy $Ge_2Sb_2Te_5$," Nat. Commun. **10**, 396 (2019).
40. A. Karvounis, B. Gholipur, K. F. MacDonald, and N. I. Zheludev, "All-dielectric phase-change reconfigurable metasurface," Appl. Phys. Lett. **109**, 051103 (2016).
41. W. Dong, H. Liu, J. K. Behera, L. Lu, R. J. H. Ng, K. V. Sreekanth, X. Zhou, J. K. W. Yang, and R. E. Simpson, "Wide bandgap phase change material tuned visible photonics," Adv. Funct. Mater. **29**, 6 (2019).
42. D. T. Pierce and W. E. Spicer, "Electronic structure of amorphous Si from photoemission and optical studies," Phys. Rev. B **5**, 3017–3029 (1972).
43. D. Arslan, K. E. Chong, D. N. Neshev, T. Pertsch, Y. S. Kivshar, and I. Staude, "Silicon Huygens' metasurfaces at oblique incidence," in *European Conference on Lasers and Electro-Optics and European Quantum Electronics Conference* (2017), paper EH_6_2.
44. Y. H. Ko and R. Magnusson, "Wideband dielectric metamaterial reflectors: Mie scattering or leaky Bloch mode resonance?" Optica **5**, 289–294 (2018).
45. C. D. Wright, Y. Liu, K. I. Kohary, M. M. Aziz, and R. J. Hicken, "Arithmetic and biologically-inspired computing using phase-change materials," Adv. Mater., **23**, 3408–3413 (2011).
46. J. Siegel, C. N. Afonso, and J. Solis, "Amorphization dynamics of Ge2Sb2Te5 films upon nano-and femtosecond laser pulse irradiation," J. Appl. Phys. **103**, 023516 (2008).
47. K. Sokolowski-Tinten, J. Solis, J. Bialkowski, J. Siegel, C. N. Afonso, and D. von der Linde, "Dynamics of ultrafast phase changes in amorphous GeSb films," Phys. Rev. Lett. **81**, 3679 (1998).
48. C. Rios, P. Hosseini, R. A. Taylor, and H. Bhaskaran, "Color depth modulation and resolution in phase-change material nanodisplays," Adv. Mater. **28**, 4720–4726 (2016).
49. S. Garcia-Cuevas Carrillo, L. Trimby, Y.-Y. Au, V. K. Nagareddy, G. Rodriguez-Hernandez, P. Hosseini, C. Rios, H. Bhaskaran, and C. D. Wright, "A nonvolatile phase-change metamaterial color display," Adv. Opt. Mater. **7**, 1801782 (2019).
50. P. Hosseini, C. D. Wright, and H. Bhaskaran, "An optoelectronic framework enabled by low-dimensional phase-change films," Nature **511**, 206–211 (2014).
51. J. R. Devore, "Refractive indices of rutile and sphalerite," J. Opt. Soc. Am. **41**, 416–419 (1951).
52. L. Trimby, "Phase-change meta-devices for tuneable bandpass filtering in the infrared," Ph.D. Thesis (University of Exeter, 2019).

159.54.42.232 {ts '2024-06-28 19:54:14'}